A modal overview of the unsteady loads induced by the Ariane-5 base-flow.

Simon Marié⋆*, Hadrien Lambaré*⋆⋆ *& Philippe Druault*⋆

⋆*Institut Jean Le Rond d'Alembert - UPMC-Paris6*
case 162, 4, Place Jussieu 75252 Paris Cedex 05

⋆⋆*CNES*
Rond-Point de l'Espace - Courcouronnes - 91023 Evry cedex - France

1. Introduction

The rear-part of Ariane 5 rocket is the home of complex phenomena potentially involving loads on the main nozzle. In particular, during transonic flight, space launchers after-bodies are subjected to significant loads acting normally to the thrust. These dynamic loads are caused by fluctuating pressure induced by a massively detached and turbulent flow. Thus, knowledge and control of these loads are of primary importance for the mechanical design of the launcher. This problem is well known in the literature and a lot of studies has been experimentally [4, 2, 11, 17] and numerically [16, 12] investigated on axisymmetric step flows. The goal of this study is to present some results for the real Ariane 5 configuration. Recently, some wind-tunnel tests have been made on a 1/60 scaled model of the real Ariane 5 rocket for a deeper understanding of the phenomenon. This study presents a physical assessment of the wind-tunnel tests made on two particular configurations. The results are mainly obtained from unsteady kulites transducers and PIV data. First, a global approach of the flow is presented to highlight the physical phenomenon. Then a POD decomposition is made on both pressure and velocity data to understand the correlation between the unsteady pressures and the velocity field.

2. Physical overview

2.1 Test and Geometry

This work is based on the wind-tunnel tests made in NLR (Netherlands) [1, 5] in 2010. The most critical part of the geometry for side-loads considerations is located on the engine nozzle and the PTM (engine thermal protection). These parts have been instrumented with a total of 112 unsteady kulites distributed along 8 rings on a 1/60 scaled model of the real Ariane 5 rocket (Fig.1). Three additional rings are located in the upper part of the after-body. For this study, we will consider the tests made for a Mach number of 0.8 with a null incidence ($\alpha = \beta = 0$). The fluctuating pressure is recorded during a period of 2.56 seconds sampled at $12800Hz$.

In previous work [10], different configurations have been investigated and physically studied in order to quantify the influence of the geometry. It has been shown that a simple configuration without the protuberances (tanks, tubes...) was able to handle the most important and critical phenomenon observed on the real geometry. This configuration will be referred as the *SMOOTH configuration* in the following. This geometry is presented on fig.2 and will be compared to the *CLEAN configuration* which is a similar geometry but where the DAAR struts have been removed. The *CLEAN configuration* has been designed first to fit the geometry of the numerical simulations performed by ONERA [15], and then to understand the influence of the DAAR struts on the after-body flow.
These two configurations will be compared in all the physical investigations of this study (In the CNES nomenclature the SMOOTH configuration is referred as the number 3310 and the CLEAN one as the number 3330. These numbers could be found in some figures). The choice of these configurations is motivated by the fundamental differences of loads induced by each flow on the after-body. This aspect will be further discuss in the following.

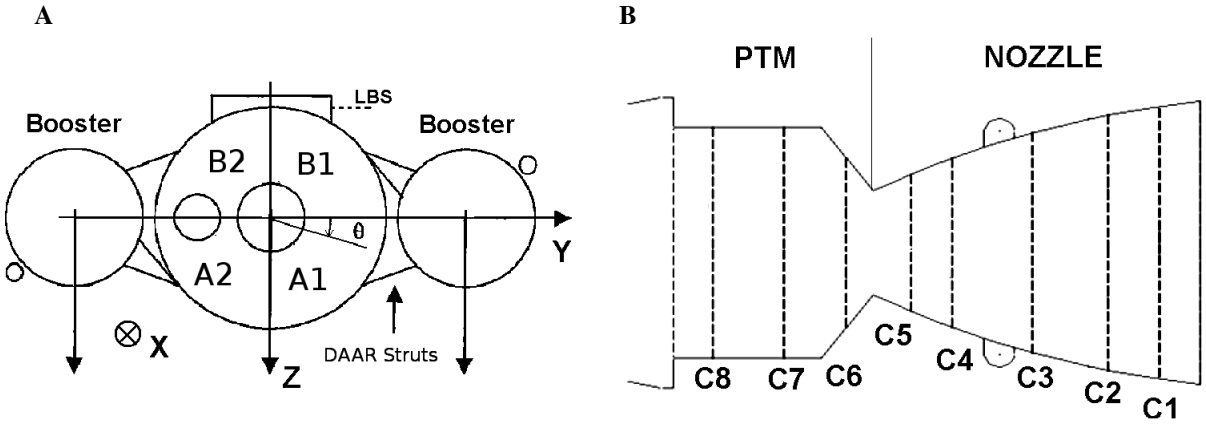

Figure 1: ***A*** *Rear view of the geometry and axes of the model. Parts A1 to B2 are identified here for further understanding of the geometrical analysis.* ***B*** *Position of sensors rings.*

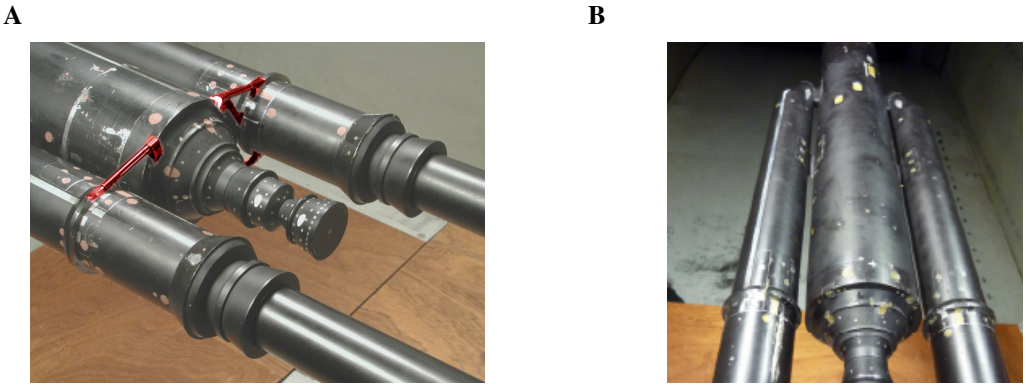

Figure 2: ***A****) The SMOOTH Configuration in the NLR wind tunnel.* ***B****) The CLEAN Configuration in the NLR wind tunnel.*

2.2 Global approach

The first way to study the unsteady side-loads induced by the turbulent flow is to compute directly the global load acting on the nozzle. The direct experimental measurement of this quantity is very difficult and demanding [4], therefore it could be useful to get this information from the kulite transducers by integrating the pressure along the nozzle:

$$\mathbf{F}(t) = \int_0^{2\pi} \int_0^L p(x,\phi,t) r(x) \mathbf{n} dx \, d\phi \equiv \sum_{i=1}^{N_c} p_i(t) \mathbf{dS}_i \tag{1}$$

where **dS** is the surface surrounding each sensors. In this work, all the integrated loads will refer to the 8 first rings of sensors (*i.e* on the Nozzle and PTM) and will be computed with the 112 corresponding kulites. The surfaces can define the order of the load that we want to compute. Indeed, in order to compute an excitation which can stress a particular structural mode of the nozzle, it can be useful to define the first-order load with (1) and $\mathbf{dS} = [S] \left\| \begin{array}{c} cos(\theta) \\ sin(\theta) \end{array} \right\|$ and the second-order load with (1) and $\mathbf{dS} = [S] \left\| \begin{array}{c} cos(2\theta) \\ sin(2\theta) \end{array} \right\|$

The validity of such an integration depends on the number of sensors involved in the experimental process [9]. A simple way to check the integration validity is to observe the decay of the azimuthal modes obtained by the spatial Fourier series decomposition of the power spectral density (PSD) $G(\theta, f)$ of the fluctuating pressure along a ring:

$$\mathbf{G}(\theta, f) = a_0 + \sum_{m=1}^{\infty} \alpha_m(f) \cos m\theta + \beta_m(f) \sin m\theta \tag{2}$$

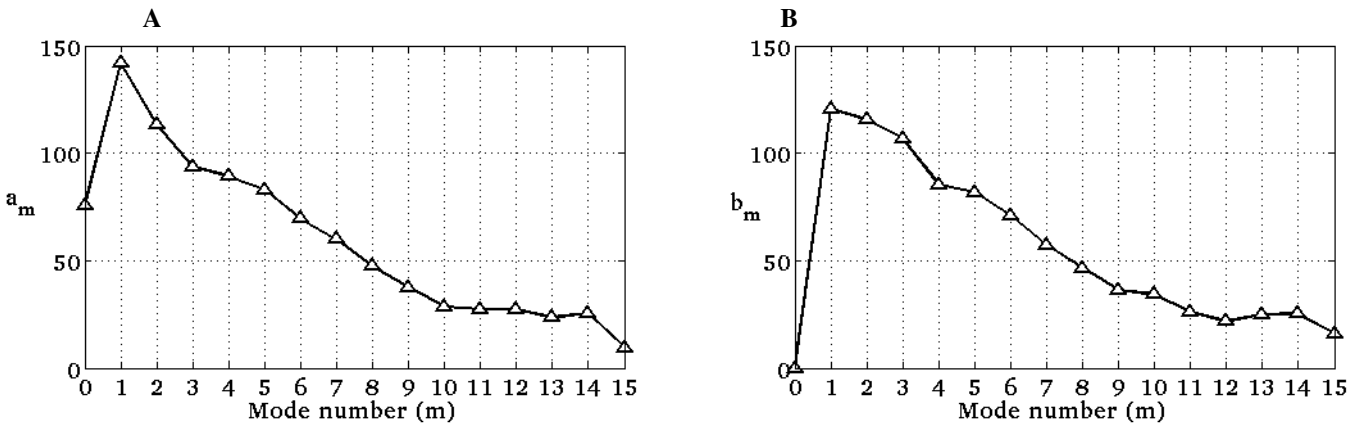

Figure 3: *Amplitude of the azimuthal modes.* ***A*** *y-modes.* ***B*** *z-modes.*

From a structural point of view, the mechanical response of the structure is characterized by a pendulum mode around 10Hz and an ovalization mode around 25Hz (frequencies refers to scale 1). So the aerodynamic excitation should be evaluated around the same frequency range. With these considerations, let define $a_m = \int_{f_1}^{f_2} \alpha_m(f)df$ and $b_m = \int_{f_1}^{f_2} \beta_m(f)df$ with $f_1 = 5$Hz and $f_2 = 40$Hz. The evolution of these coefficients is shown on Fig.3. The decrease of the mode amplitude allow us to use equation (1) to characterize the unsteady loads between 5 and 40Hz. The PSD of these loads are presented on Fig.4 for CLEAN and SMOOTH configurations.

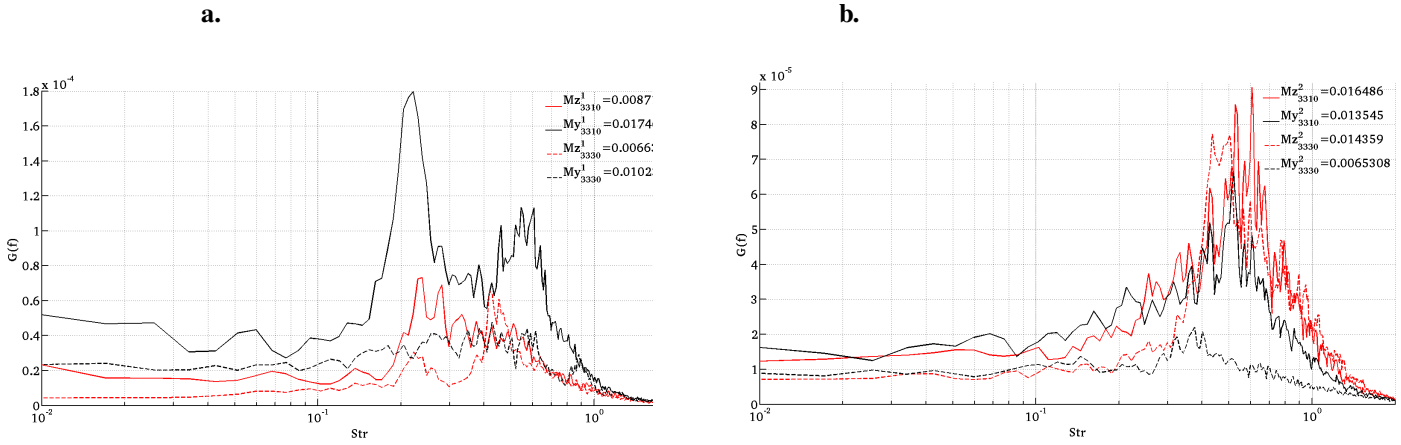

Figure 4: *a. PSD of y-load induced by the* $m = 1$ *mode. b. PSD of y-load induced by the* $m = 2$ *mode. Dashed lines are for CLEAN configuration and Filled line for SMOOTH configuration. These curves are voluntarily set with arbitrary units*

In order to clarify the notation in the following, the $m = 1$ excitation will be referred as the first order load and the $m = 2$ to the second order load.
First, one can notice that the first order load is characterized by a peak around $Str = 0.2$ (= 10Hz at Mach= 0.8) and a broad-band load around $Str = 0.5$. Moreover, the second order load exhibits a broad-band load around $Str = 0.5$. This means that the aerodynamic excitation fits the mechanical response of the structure (pendulum mode and ovalization mode). This explains why the phenomenon is so important and could be damaging for the launcher. Then, we observe that the CLEAN configuration (where the DAAR struts have been removed) induces a weaker load around $str = 0.2$. This means that the DAAR struts play an important role on the unsteady loads acting on the nozzle. These first global differences in the load induced by two different geometry are of primary importance for the understanding of the phenomenon. But a local analysis has to be investigate in order to link the effect of the DAAR struts on the flow to the unsteady loads induced by this flow.

2.3 Local approach

Another way to study the buffeting phenomenon is to look at the pressure PSD repartition along the geometry of the rear-body. Let $G_p(\theta, x, f)$ be the pressure PSD at the point $[x, \theta]$. The quantity $f^\star(\theta, x)$ such as:

$$G_p(\theta, x, f^\star) = max[G_p(\theta, x, f)] \tag{3}$$

is a way to study the local frequency behavior of the phenomenon. Fig.5 represents $f^\star(x, \theta)$ for the CLEAN and SMOOTH configurations. The SMOOTH configuration presents two particular areas ($25° \leq \theta \leq 100°$and $220° \leq \theta \leq 300°$) where the maximal PSD are characterized by frequencies around 25Hz. This phenomenon could be interpreted as the consequences of the reattachment flow in these areas. Moreover, 10Hz frequencies ($Str = 0.2$ at Mach= 0.8) are observed in the overall geometry and are the signature of a global shedding phenomenon. For the CLEAN configuration, the pressure PSD maxima are weaker and organized in a smaller area. Moreover, the characteristic frequencies are distributed along 25 Hz on a large area whereas the 10 Hz phenomenon is restricted to the upper part of the rear-body.

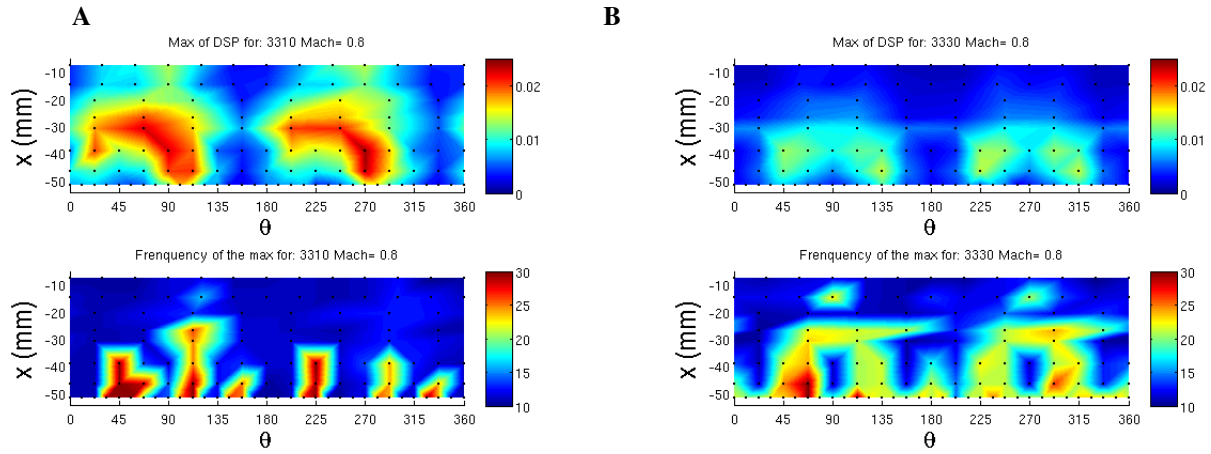

Figure 5: *Frequency repartition of the maximal PSD along the nozzle and the PTM. Color scale refers to the frequency in Hz.*

This kind of frequency information allow the identification of the phenomenon responsible for the different part of the load PSD observed on Fig.4. But one information is missing to fully describe the unsteady pressure repartition on the Nozzle. This information is related to the two point correlation analysis and can give reliable informations on the local flow organization. Fig. 6 displays the phase of the two point coherence for the 112 unsteady pressures located on the critical part of the nozzle.

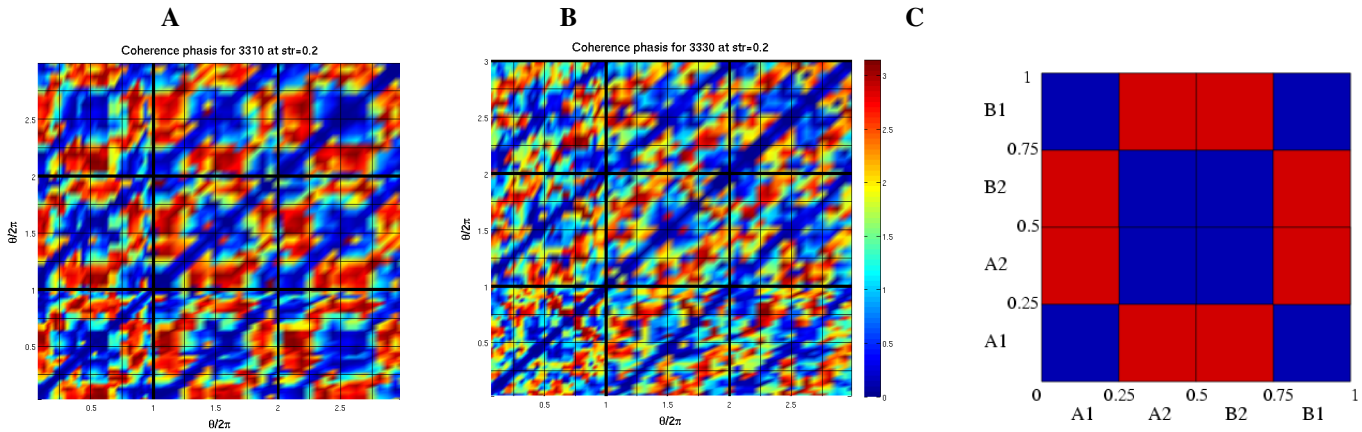

Figure 6: *Phase of the coherence for the two-point coherence of the three first rings of kulites.(A) SMOOTH configuration, (B) CLEAN configuration.(C) Ideal phase scheme: red parts represents a phase of π blue parts, a phase of 0.*

The phase of the two different configuration clearly indicates a different flow topology. If we refer to the ideal phase scheme presented on fig.6C the SMOOTH configuration exhibits an organized flow with a typical phase opposition from both side of the plane normal to the booster (Z-plane) and a phenomenon in phase on both side of the other plane (Z-plane). In contrast, the CLEAN configuration does not exhibit any particular organization of the flow. Thus it seems that the peak observed around $str = 0.2$ on the Y-load of the SMOOTH configuration is related to a phenomenon with phase opposition from both side of the Z-plane. This phenomenon disappears on the CLEAN configuration and no peak is observed on the Y-load.

This local analysis has been helpful to identify some structured phenomenon in the unsteady flow and to give an *a priori* hypothesis for the differences observed on the SMOOTH and CLEAN configuration. This hypothesis has to be firstly quantified with a modal analysis of the flow, where energetic and coherent structures could be distinguished and identified.

3. Modal overview of the flow

The application of Proper Orthogonal Decomposition to turbulent flow analysis was first proposed in 1967 by Lumley [8] as an objective method to identify deterministic features in turbulent flows. According to Lumley [8], an organized flow structure called coherent structure is the structure that has the largest mean square projection of the velocity field. This maximization leads to a Fredholm integral eigenvalue problem (Holmes et al. [7])

$$\sum_{j=1}^{N_c} \int_S R_{ij}(\mathbf{X}, \mathbf{X}')\phi_j^{(n)}(\mathbf{X}')d\mathbf{X}' = \lambda^{(n)}\phi_i^{(n)}(\mathbf{X}), \tag{4}$$

where X indicates the space variable and $R(\mathbf{X}, \mathbf{X'})$ refers to the time averaged two point spatial correlation tensor of the flow variable. In this equation, ϕ denotes the spatial orthogonal eigenfunctions and λ is the corresponding eigenvalue. Such equation provides a finite discrete number of POD eigenfunctions, $\phi^{(n)}$ with n varying from 1 to N_{mod} which is the total number of POD modes corresponding to the dimension of the spatial correlation matrix. Based on this flow decomposition each instantaneous fluctuating velocity field (for instance the u velocity component) can then be expressed as follows:

$$u_i(\mathbf{X}, t) = \sum_n a^{(n)}(t)\phi_i^{(n)}(\mathbf{X}), \tag{5}$$

where $a^{(n)}(t)$ is the nth random temporal coefficient of projection of $u(\mathbf{X}, t)$ onto the nth POD eigenfunction $\phi^{(n)}(\mathbf{X})$ and Nmod is the total number of the POD decomposition. The presented method is the classical representation of POD problem. In this method the kernel of the integral eigenvalue problem is the time averaged two-point spatial correlation tensor. In 1987, Sirovich [14] developed an equivalent method called snapshot POD. This process leads to a new Fredholm equation. The kernel of this Fredholm equation is based on a spatial averaging. The eigenfunctions resulted from the snapshot formulation are $a^{(n)}(t)$. These temporal functions are mutually orthogonal: $\overline{a^{(n)}(t)a^{(m)}(t)} = \delta_{nm}$, with δ the Kronecker symbol. The $\phi_i^{(n)}(\mathbf{X})$ are determined by the projection of the velocity field onto the temporal eigenfunctions.
For this study, a Proper Orthogonal Decomposition will be applied to the unsteady pressure field and to the unsteady velocity field in order to identify the energetic coherent structures and their influence on the nozzle load.

3.1 Pressure modes

The application of eq.5 to the unsteady pressure field can give us informations about the energetic repartition of the pressure signal. The most energetic pressure modes are shown in appendix 1. This representation shows the spatial repartition of the quantity $\sqrt{\lambda_n}\phi^{(n)}(x, \theta)$, where λ_n is the n^{th} eigenvalue associated to the eigenfunction $\phi^{(n)}(x, \theta)$. It can be seen that the first pressure mode of the SMOOTH configuration induces a positive pressure contribution on part A1 and B1 ($0 < \theta < 90$ and $270 < \theta < 360$) and a negative contribution on part A2 and B2. These contributions are favorable to the structural pendulum mode which corresponds to a local displacement of the nozzle. Moreover, the second pressure mode of the SMOOTH configuration induces a positive pressure contribution on part A1 and B2 ($0 < \theta < 90$ and $180 < \theta < 270$) and a negative contribution on part A2 and B1 which are favorable to the structural ovalization mode which corresponds to a local deformation of the nozzle. These first assessments indicate that the first two pressure POD modes contain the main effects of the pressure on the nozzle. The situation is reversed for the CLEAN configuration. Indeed, the first pressure POD mode is favorable to the ovalization mode and the second to the

pendulum mode. Despite this reversion, the principal difference with the SMOOTH configuration remains the intensity of the eigenfunctions. Indeed, the lower level of these functions for the CLEAN configuration induces less contrasted phenomena. Moreover, for the SMOOTH configuration, the first two modes contain 23% of the total energy against 16% for the CLEAN configuration.

From a formal point of view, we can evaluate the contribution of the POD modes to the unsteady loads computed with eq.1. Let define $\widehat{F_k^m}$ and $\tilde{F}^m$ the unsteady loads induced by the pressure $\widehat{p_k^m}$ and $\tilde{p}^m$ defined as:

$$\widehat{p_k^m}(\mathbf{X}, t) = \sum_{n=k}^{m} a^{(n)}(t)\phi^{(n)}(\mathbf{X}) \tag{6}$$

$$\tilde{p}^m(\mathbf{X}, t) = a^{(m)}(t)\phi^{(m)}(\mathbf{X}) \tag{7}$$

Then, $\tilde{F}^1$ represents the load induced by the first POD mode of the pressure and $\widehat{F_3^{112}}$ represents the load induced by the pressure field projected onto POD modes from 3 to 112. Fig.7 and 8 display the PSD of $\tilde{F}^1$, $\tilde{F}^2$ and $\widehat{F_3^{112}}$ for SMOOTH and CLEAN configurations respectively.

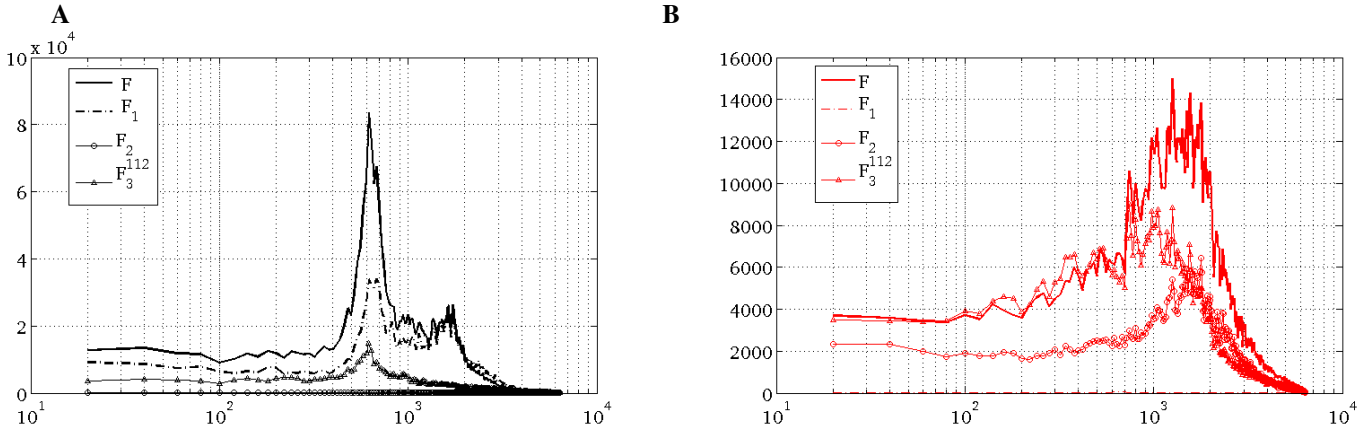

Figure 7: *Contribution of the POD modes to the integrated (A) first-order load and (B) second order load on the SMOOTH configuration.*

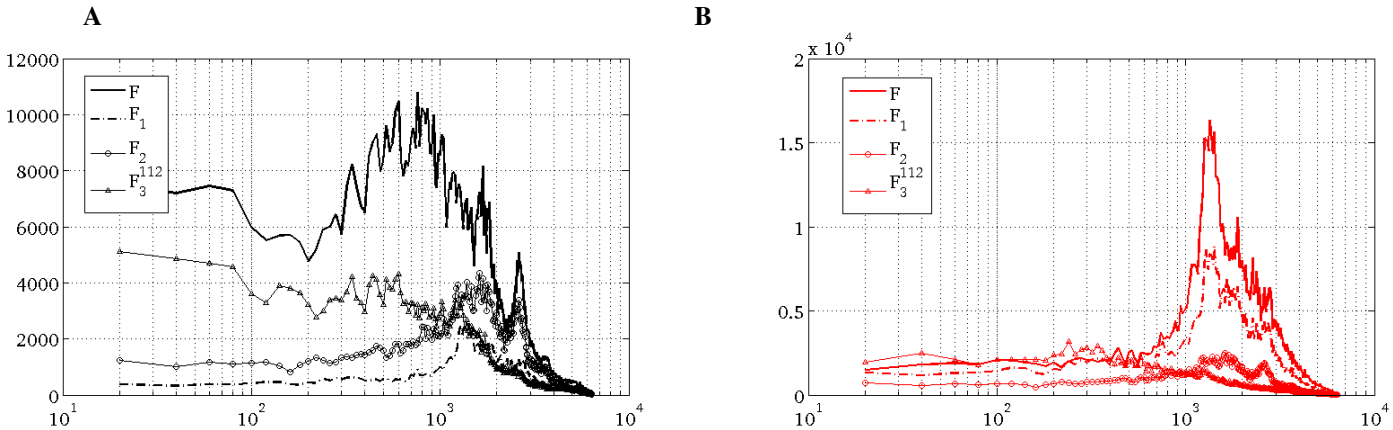

Figure 8: *Contribution of the POD modes to the integrated (A) first-order load and (B) second order load on the CLEAN configuration.*

For the SMOOTH configuration, the PSD is dominated by the contribution of $\tilde{F}^1$ which displays the main frequency shape of the total PSD load. This means that the first pressure POD mode contains the main phenomenon responsible for the first-order load (Fig.7A). This is strengthened by the fact that the second POD mode does not contribute at all to the first-order load. In the same way, the first POD mode does not contribute to the second-order load (Fig.7B). However, the domination of the second POD mode is not so obvious for the second order load, and the higher POD modes seem to add an important contribution to the PSD frequency shape.

For the CLEAN configuration, the PSD contribution of the POD modes are also in agreement with the previous considerations. The first POD mode is linked with the second-oder load and the second POD mode is linked to the first-order load. However, for this configuration, the higher POD modes have a non negligible influence on the load and both of the first two POD modes are involved in the load.

Thus, Proper Orthogonal Decomposition of the pressure field has highlighted that the main phenomenon responsible for the unsteady load acting on the nozzle is contained in the first two energetic POD modes. The main difference between SMOOTH and CLEAN configurations hold in the structured and organized phenomena which are perfectly identified for the SMOOTH configuration, and less stressed for the CLEAN configuration.

3.2 Velocity modes

For the wind tunnel tests performed in 2010, Particle Image Velocimetry measurement were investigated in order to get some information about the velocity field. This PIV was time-resolved with a sample frequency of 2700Hz and $Nt = 2728$ timesteps [13]. The acquisition was made in the plane orthogonal to the booster (Z-plane). In this study, we will focus on the unsteady part of the velocity. Thus the averaged velocity will be subtracted to the main field in order to use only the fluctuating part of the velocity field.

The weakness of the frequency sampling of the PIV data (2700Hz) compared to the typical frequency of the phenomenon highlighted in the previous sections ($\sim 500Hz$ on the 1/60 scale model) makes the spectral analysis of the velocity field impossible. Indeed, some aliasing phenomenon will disturb the Fourier decomposition of the velocity signal. Despite this aliasing problem, the Proper Orthogonal Decomposition provides reliable informations about the coherent structures of the velocity field. In eq.4, $R(\mathbf{X}, \mathbf{X'})$ refers to the time averaged two point spatial correlation tensor. Thus POD analysis of the velocity field will not be corrupted by the low-frequency used for PIV sampling.

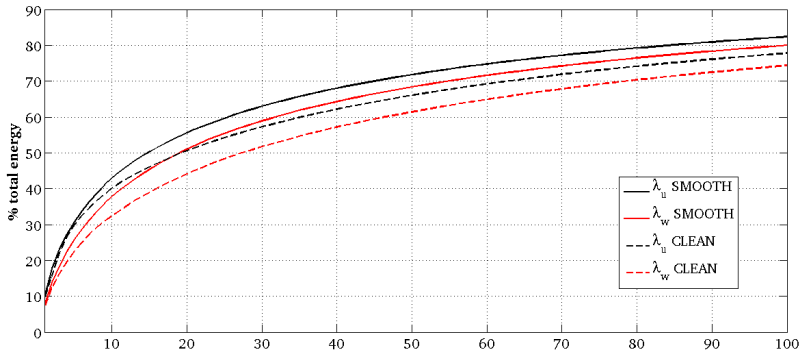

Figure 9: *Evolution of the cumulated percentage of the total energy with the number of modes.*

Fig.9 show the number of modes needed to achieve a given percentage of the total energy. The total number of nonzero velocity modes is 2728 (the rank of the input matrix) but according to fig.9, 80% of the energy is contained in the first 100 modes. Moreover, Epps [3] has shown that beyond a certain number of modes obtained from PIV data, the observed energy was only due to a random noise of the data. This Epps criterion indicates that for our PIV data, the POD modes beyond 500 are not to be taken into account.

The most energetic velocity modes obtained with the Proper Orthogonal Decomposition of the velocity field are shown in appendix 2. This representation shows the spatial repartition of the quantity $\sqrt{\lambda_n}\phi^{(n)}(x,z)$, where λ_n is the n^{th} eigenvalue associated to the eigenfunction $\phi^{(n)}(x,z)$. The first observed modes display the larger coherent structures which correspond to a macro-movement of the flow.

Because we want to focus on the physical causes of the unsteady loads acting on the nozzle, a simple velocity analysis is not sufficient for a global understanding. Thus, the principal information remains in the correlations between the velocity field and the pressure data.

3.3 Pressure/Velocity Correlation

The modal analysis of pressure and velocity fields has given some information about the energy repartition. Now, further investigations have to be made to understand how the coherent structures of the velocity field are impacting the nozzle and inducing the observed unsteady loads. Moreover, a crucial point is to understand if some pressure modes are linked to a particular structure of the flow and where does this link comes from. The idea is to use here both of the classical correlation techniques and the POD analysis in order to extract the relevant information from pressure and velocity fields. The basic correlation coefficient is defined by:

$$C(\mathbf{X}) = \frac{\overline{p(x,t).U(x,t)}}{\sigma_p \sigma_u} \tag{8}$$

where $\overline{...}$ denotes the time averaging operator and σ the standard deviation. With this normalization, we have: $C(\mathbf{X} \in [-1\ 1]$. This definition supposes that $p(x,t)$ and $U(x,t)$ are known at the same moments. During the acquisition, pressure and velocities have been synchronized in order to have the same starting point for pressure and velocity signals. However, the pressure sampling frequency is 12.8KHz and the velocity sampling frequency is 2.7KHz. Thus, the only way to get a reliable correlation coefficient is to subsample the pressure signal and to interpolate this signal on the velocity time base. Then we obtain pressure and velocity signals of one second sampled at 2700 Hz. It is important to note here that we do not include any pressure filter in this procedure in order to keep the overall energy of the pressure signal. Indeed, as we do not proceed to any Fourier transform of the pressure, but only to the correlation coefficient, the sub-sampling has only small effects on the observed overall RMS values.

Once the pressure sampling fitted to the velocity, a focusing point is to choose the quantity to be correlated to the velocity. Indeed, if we compute the basic correlation coefficient, we have to choose some special pressure points in the plane concerned by the velocities (*i.e* the Z-plane). But another idea, is to correlate directly the velocity to the global integrated load. Then, in eq.8 the pressure must be replaced by $Fy(t)$ or $Fz(t)$ where F can be the first-order or second-order load integrated with the sub-sampled pressures. This method is well adapted to the understanding of the interaction between the velocity field and the characteristic quantity represented by the unsteady load. In the following, the correlation coefficient will be written with subscript an superscript to distinguish the correlated quantity. Then, $C^u_{Fz}(\mathbf{X})$ will be the correlation coefficient between the Z-load and the U velocity component.

Because very few informations are known about the pressure/velocity correlations, we cannot *a priori* know the typical value of such a quantity. Then an intuitive way is to find the maximum of correlation obtained with some parameter variation. The first parameter is the time-delay between pressure and velocity. This parameter is introduced in the pressure signal by substituting $F(t)$ by $F(t+\tau)$.

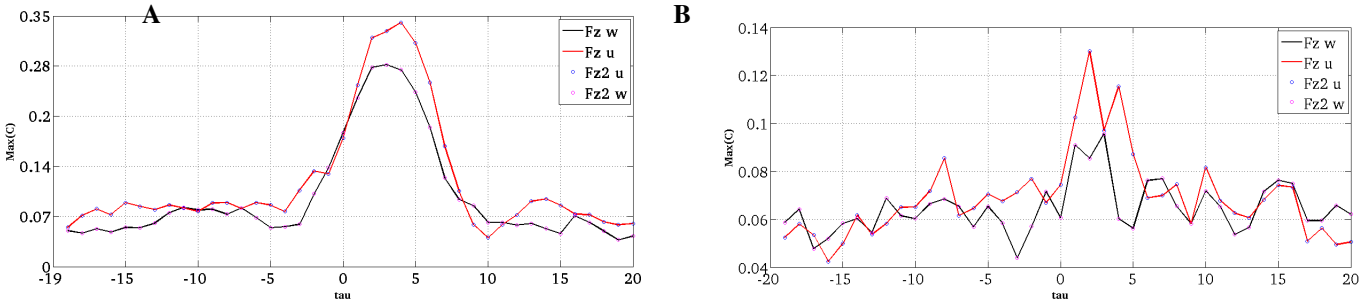

Figure 10: *Evolution of the maximum correlation max*$[C(\boldsymbol{X})]$ *with the parameter* τ *given in number of time step. O value correspond to the synchronization top. A) SMOOTH configuration, B) CLEAN configuration. (F refers to the first-order load and F2 to the second-order load).*

Fig.10 show that a delay of 4 timestep induces the maximum of correlation. This corresponds to a time delay of 0.31ms and a space interval of 42.5mm based on a convection speed of $U_0/2 \sim 136$m/s. The SMOOTH configuration exhibits a maximum of 0.33 correlation and the CLEAN configuration, a maximum of 0.13. The maximum of correlation is observed in both cases between the Z-load and the u-component of the velocity. In the following, all the correlations will be computed with $\tau = 4\Delta t$

Another way to increase the computing accuracy of the correlation coefficient is to use the physical assessments exposed

in the modal overview of the flow. Indeed, it has been shown that the most energetic POD modes of the pressure and the velocity were playing an important role in the flow physics. Then we can wonder if the correlation coefficient will change if we consider only the most energetic modes in the correlation. In the same idea that in §3.1, we can define:

$$[\widehat{C_F}]_k^m(\mathbf{X}) = \overline{\frac{\widehat{F_1^m}(\mathbf{X},t).\widehat{U_1^k}(\mathbf{X},t)}{\widehat{\sigma_p}\widehat{\sigma_u}}} \tag{9}$$

where $\widehat{F_1^m}(\mathbf{X},t)$ define the load integrated with only the m first pressure POD modes and $\widehat{U_1^k}(\mathbf{X},t)$ is the projection of the velocity signal onto the first k POD modes. (Cf eq.6). Then the parameter m refers to the number of POD modes considered for pressure and the parameter k to the velocity modes.

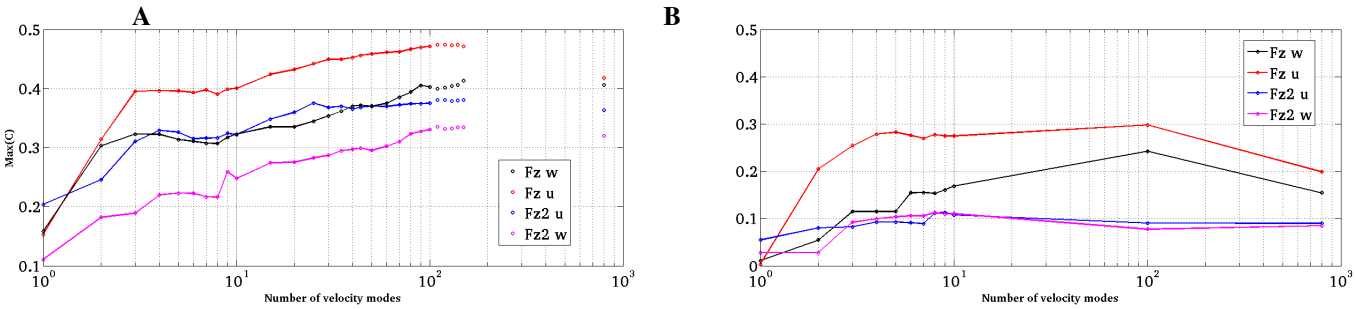

Figure 11: *Evolution of the maximum correlation* $max(\left\|[\widehat{C_F}]_k^2(\boldsymbol{X})\right\|)$ *with the parameter k. A) SMOOTH configuration, B) CLEAN configuration.*

According to the pressure mode analysis, the parameter m of eq.9 will be taken to 2. Fig.11 show the evolution of the maximum correlation with the parameter k. These curves clearly indicates that the first velocity POD modes are the most correlated to the evolution of the load induced by the first two pressure modes. Moreover, the slope of these curves remains high for $k = 1 \rightarrow 5$. The correlation coefficients shown in appendix 3, consider these first five modes for the velocities signals. With these modes, a maximum of 0.45 is reached for the SMOOTH configuration in the area of the base-flow. The gap between correlations on the SMOOTH configuration and the CLEAN one is in agreement with considerations of section 2.3. Indeed, the presence of the DAAR struts on the SMOOTH configurations seems to induce an organized and coherent flow which lead to a local excitation that fit the mechanical response of the structure. In contrast, the absence of DAAR struts on the CLEAN configuration leads to a more anarchic flow where the energy is spread over multiple structures which are note correlated to the pressure. For a complete interpretation of these flows, some frequency information in the velocities are missing. Indeed, it would be helpful to know the velocity frequencies which are correlated to the pressure. The only thing we can do is to use the frequency informations of the pressure.

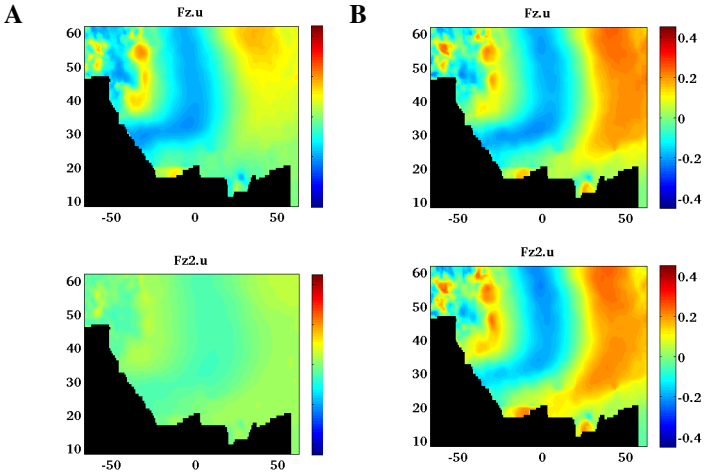

Figure 12: *Correlation coefficient* $[\widehat{C_{Fz}^u}]_5^2(\boldsymbol{X})$. *Fz has been integrated with filtered pressure around A) str* = 0.2 *and B) str* = 0.5.

Fig.12 displays the correlations between the Z-load and the u-component of the velocity. Here, the pressure has been filtered with a pass-band filter around some characteristic frequencies. These results clearly show that the velocity field is more correlated to the mid-frequency part of the load ($str = 0.5$, fig.12B), especially for the second-order load which contains mainly a broad-band load (Cf fig.4). Moreover, the little $str = 0.2$ peak observed on the Z first-order load (Cf fig.4) seems to be correlated to the velocity field in the early detached region. This can be seen as the beginning of a proof that this $str = 0.2$ peak is induced by a global shedding phenomenon, taking its origins in the early detached flow.

4. Conclusion

The unsteady aerodynamics of the Ariane-5 after-body is the home of complex phenomenon. This work has highlighted two different geometrical configurations tested in the 2010 wind-tunnel tests. The SMOOTH configuration exhibits structured and unsteady phenomenon and has became a reference configuration for engineers. The CLEAN configuration has been designed to understand the influence of the DAAR struts on the buffeting phenomenon. A physical overview of these typical flows has shown that the struts were inducing a phase opposition phenomenon which was responsible of an important peak around $str = 0.2$ on the unsteady loads acting on the nozzle. Then the Proper Orthogonal Decomposition has been applied to the pressure and velocity fields. It has been shown that the main physics of the flow was governed by two particular pressure modes and five main velocity modes. The study of pressure/velocity correlations has highlighted the relationships between the main modes of the flow. This modal analysis has confirmed the structural influence of the DAAR struts and their contribution to the buffeting phenomenon. The main hypothesis is that the presence of the struts generate a global shedding phenomenon growing in the early detaching flow with a characteristic frequency of $str = 0.2$. Then smaller turbulent structures (higher frequencies) held by the first velocity POD modes are convected in the rear-part of the nozzle and impact the mechanical structure, inducing a broad-band load.
These first assessments about frequency correlations have to be consolidate by further experimental or numerical investigations. A PIV plane in the Y-plane could be able to increase the level of information in this area and a higher sampling frequency for the time-resolved PIV will induce a confirmation or refutation of the assessments made in this study.

Acknowledgment

The present research was performed in the framework of the ESA TRP “Unsteady Subscale Force Measurements within a Launch Vehicle Base Buffeting Environment” [6] financed by the European Space Agency. The prime contractor of this project is DLR (Germany) with membership of NLR (Netherlands), TU-DELFT (Netherlands), EADS-Astrium (France), ONERA (France) and CNES (France).

References

[1] S. David and S. Radulovic. Prediction of Buffet Loads on the Ariane 5 Afterbody. In *6th Symposium on Launcher Technologies.*, Munich, Germany, 8-11 November 2005.

[2] G.E. Dumnov. Unsteady Side-Loads Acting on the Nozzle with Developed Separation Zone. *AIAA-paper*, 96-3220, 1996.

[3] B. Epps and A. Techet. An error threshold criterion for singular value decomposition modes extracted from PIV data. *Exp. in Fluids.*, 48:355–367, 2010.

[4] F. Garcon and J.P. Drevet. Unsteady load measurements on the main engine nozzle of the Ariane 5 launch vehicle. In *Third European Symposium on Aerothermodynamics for Space Vehicles.*, page 623, ESTEC, Noordwijk, Yhe Netherlands, December 1998. ESA.

[5] E. Geurts. Steady and unsteady pressure measurements on the rear section of various configurations of the Ariane 5 launch vehicle. In *6th Symposium on Launcher Technologies.*, Munich, Germany, 8-11 November 2005.

[6] K. Hannemann, H. Ludeke, J.-F. Pallegoix, A. Ollivier, H. Lambare, J.E.J. Maseland, E.G.M. Geurts, M. Frey, S. Deck, F.F.J. Schrijer, F. Scarano, and R. Schwane. Launch vehicle base buffeting: Recent experimental and

numerical investigations. Technical report, Unsteady Subscale Force Measurements within a Launch Vehicle Base Buffeting Environment, 2011.

[7] P. Holmes, J.L. Lumley, and G. Berkooz. *Turbulence, coherent structures, dynamical systems and symmetry.* Cambridge monograph on mechanics eds., 1996.

[8] J.L. Lumley. The structure of inhomogeneous turbulent flows. In Yaglom and Tatarsky, editors, *Atm. Turb. and Radio wave Prop.*, pages 166–178, 1967.

[9] S. Marie, S. Deck, and P.E. Weiss. From pressure fluctuations to dynamic loads on axisymmetric step flows with minimal number of kulites. *Computers & Fluids*, 39(5):747–755, 2010.

[10] S. Marie and H. Lambare. On the unsteady loads induces by the bluff-body wake of the Ariane-5 launcher. In *6th IUTAM symposium on the bluff-body wake.*, Capri, Italy, June 2010.

[11] P. Meliga and P. Reijasse. Unsteady transonic flow behind an axisymmetric body equipped with two boosters. *AIAA paper*, 2007-4564, 2007.

[12] M.M. Ragab. Buffet Loads Prediction for a Launch Vehicle and Comparison to Flight Data. *J. of Spacecraft and Rockets*, 29(6), 1992.

[13] F Schrijer and F. Scarano. Experimental investigation of transonic unsteady flow phenomena in the base of the Ariane 5 using PIV and pressure measurement. In *4TH EUROPEAN CONFERENCE FOR AEROSPACE SCIENCES.*, St-Petersbourg, Russia, 04-08 July 2011.

[14] L. Sirovich. Turbulence and the dynamics of coherent structures. part i: Coherent structures. *Q. Appl. Math*, XLV:561–571, 1987.

[15] P.E Weiss and S. Deck. Zonal Detached Eddy Simulation of the flow dynamics on an Ariane 5-type afterbody. In *4TH EUROPEAN CONFERENCE FOR AEROSPACE SCIENCES.*, St-Petersbourg, Russia, 04-08 July 2011.

[16] P.E. Weiss, S. Deck, J.C. Robinet, and P. Sagaut. On the dynamics of axisymmetric turbulent separating/reattaching flows. *Physics of Fluids*, 21:075103, 2009.

[17] H. Wong, J. Meijer, and R. Schwane. Experimental and Theoretical Investigation of Base-Flow Buffeting on Ariane 5 Launch Vehicles. *J. Prop. and Power*, 23(1):116–122, 2007.

Annexe 1: Pressure POD Modes

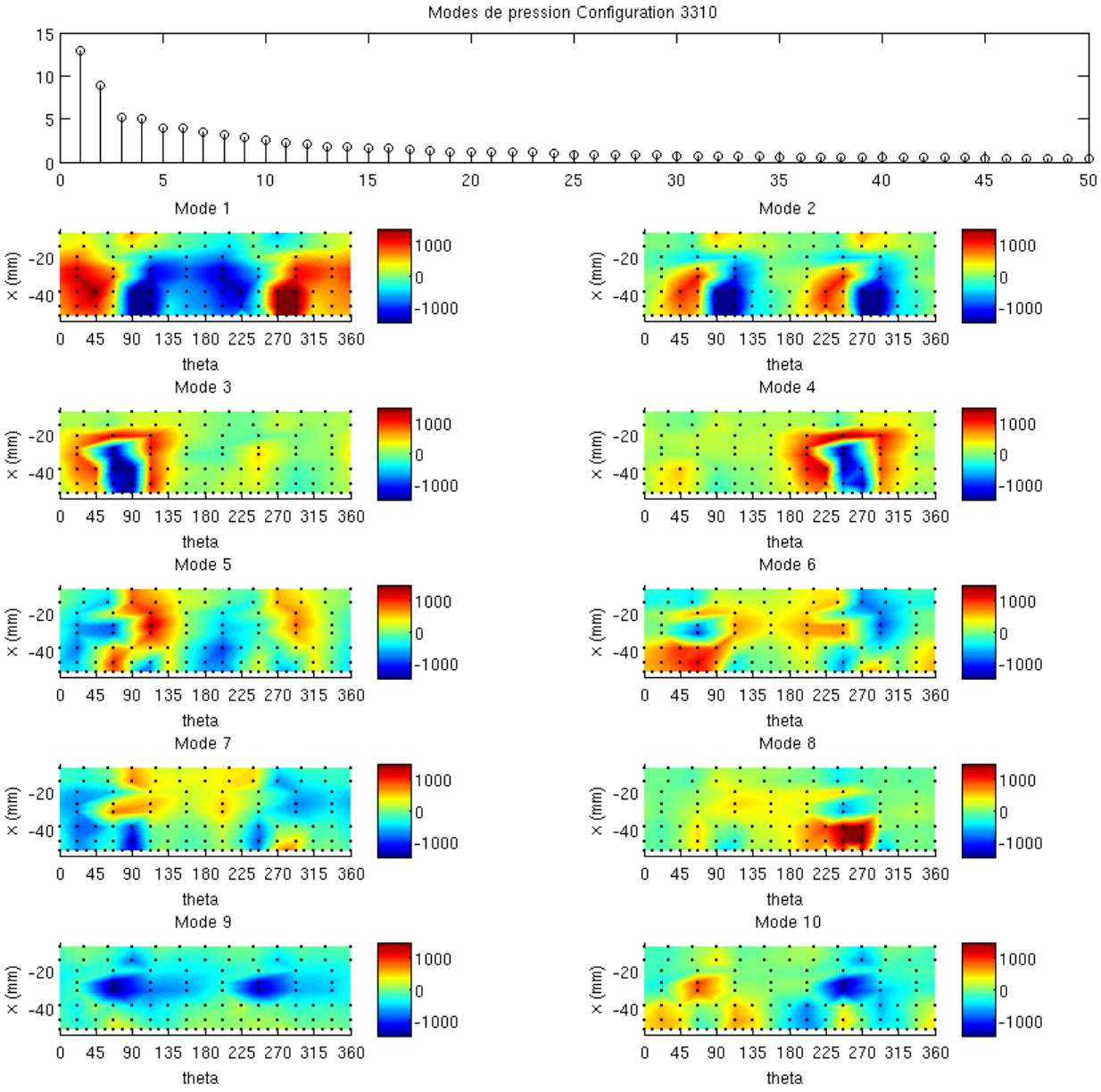

Figure 13: *Contribution (in %) of each λ_n to the total energy and Pressure POD modes for the SMOOTH Configuration.*

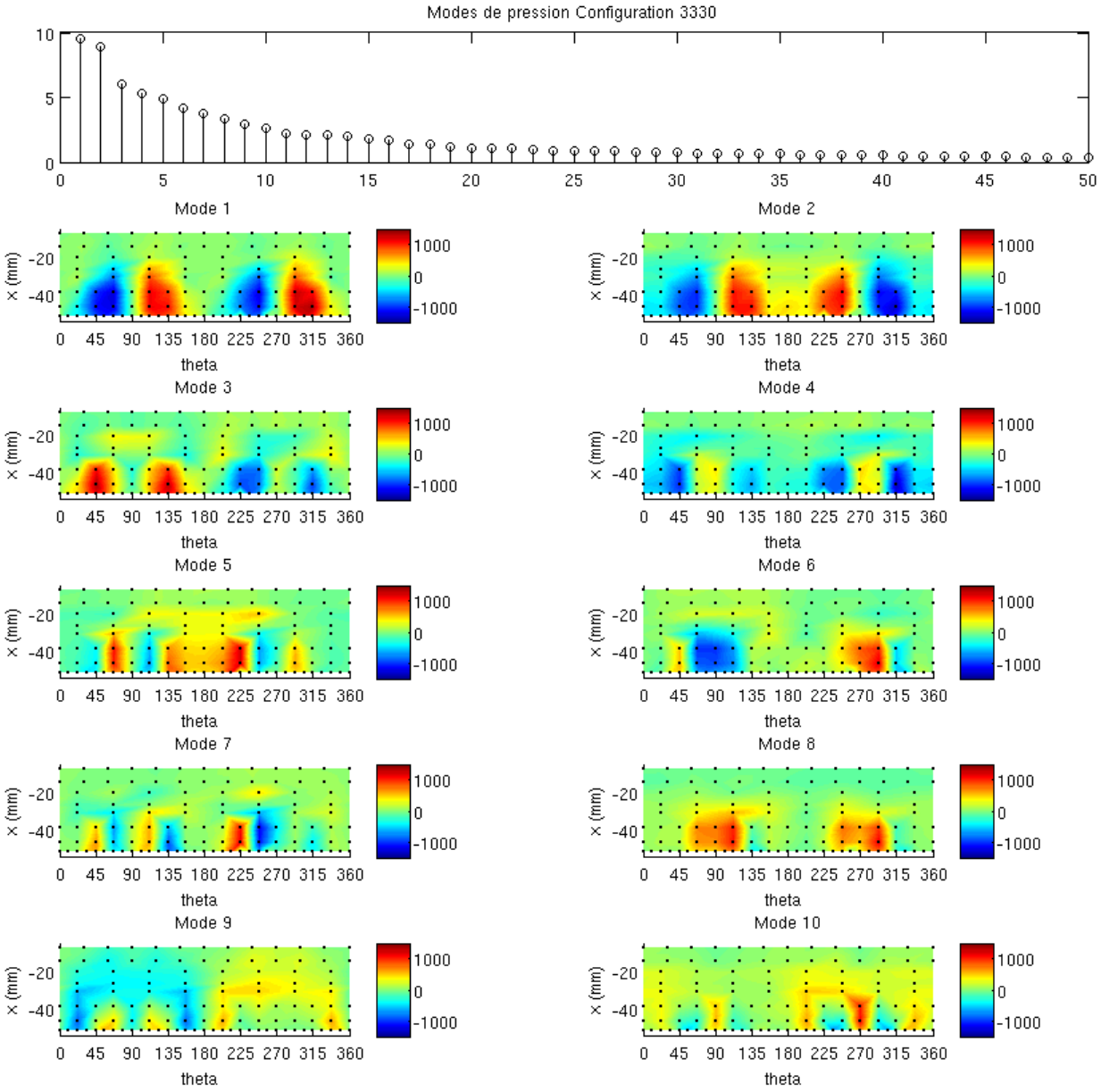

Figure 14: *Contribution (in %) of each λ_n to the total energy and Pressure POD modes for the CLEAN Configuration.*

Annexe 2: Velocity POD Modes

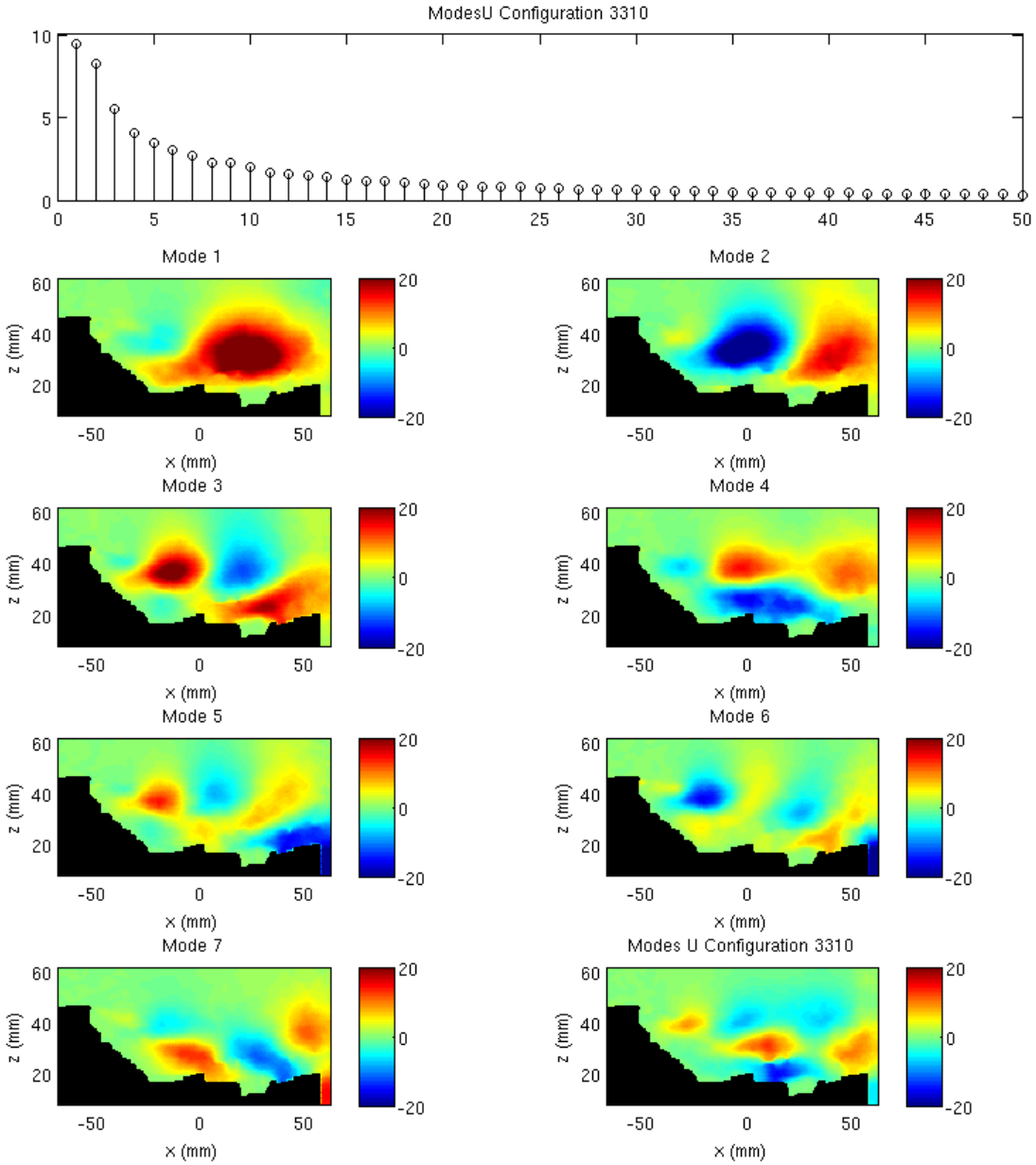

Figure 15: *Contribution (in %) of each λ_n to the total energy and U velocity POD modes for the SMOOTH Configuration.*

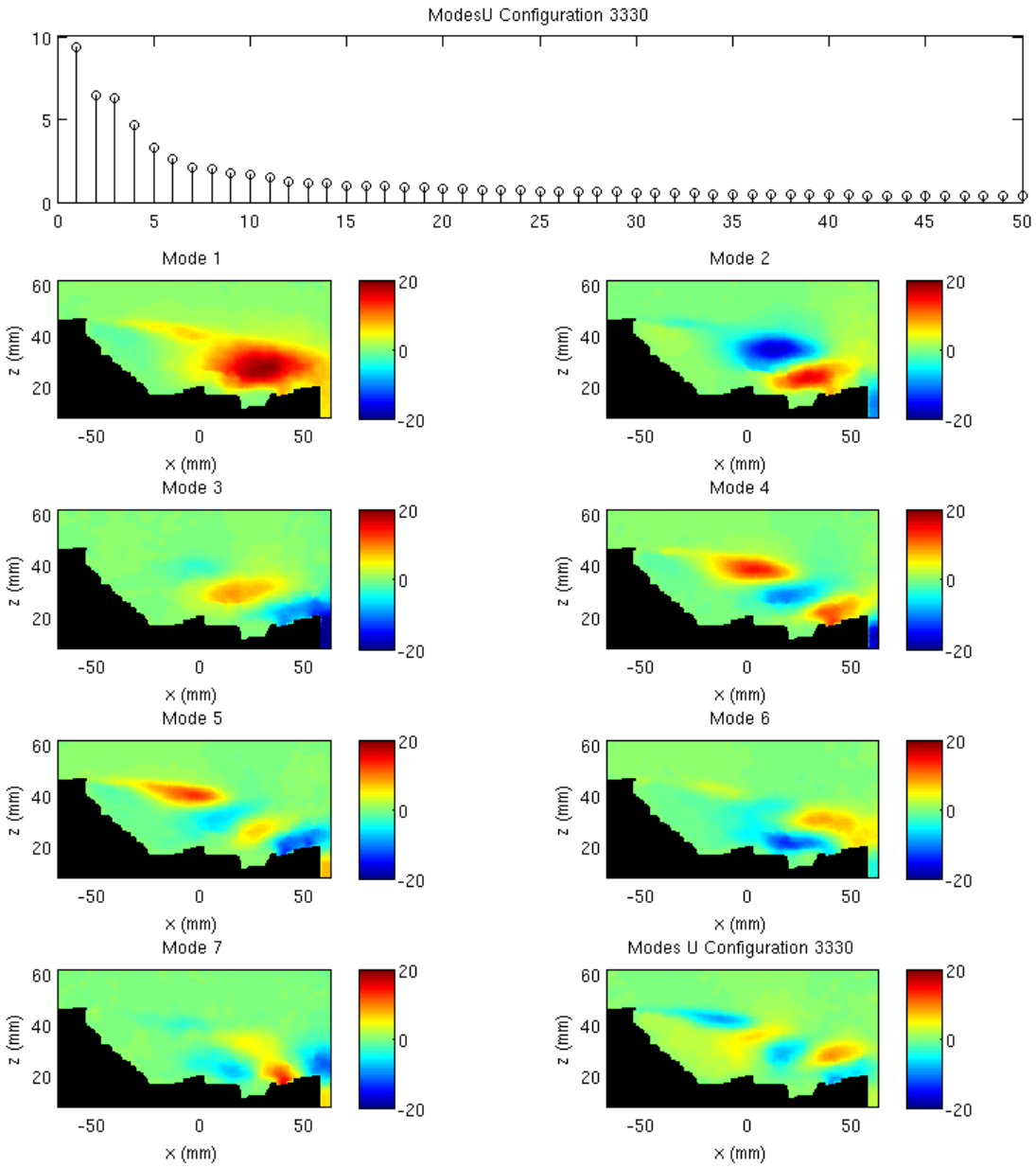

Figure 16: *Contribution (in %) of each λ_n to the total energy and W velocity POD modes for the CLEAN Configuration.*

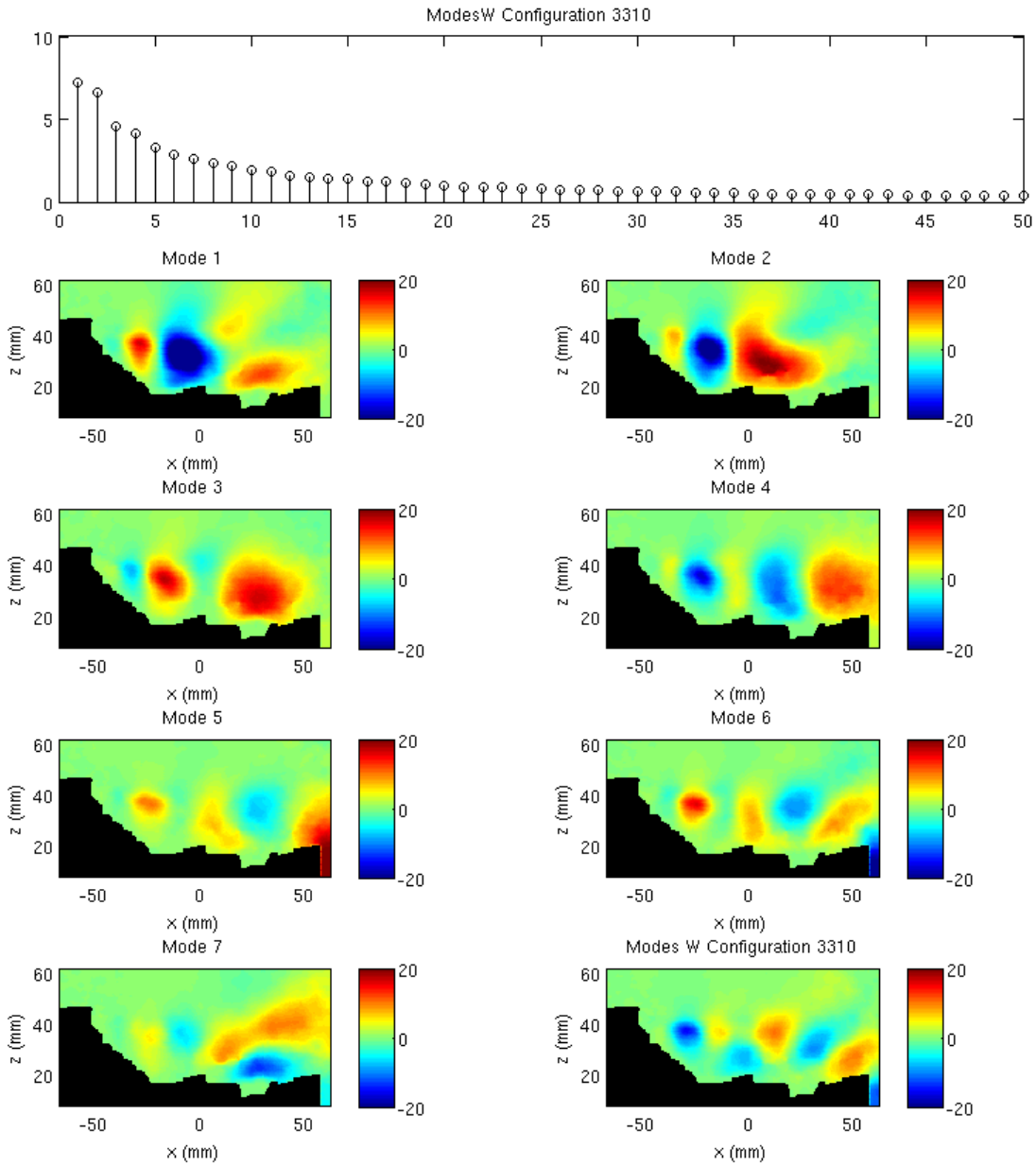

Figure 17: *Contribution (in %) of each λ_n to the total energy and W velocity POD modes for the SMOOTH Configuration.*

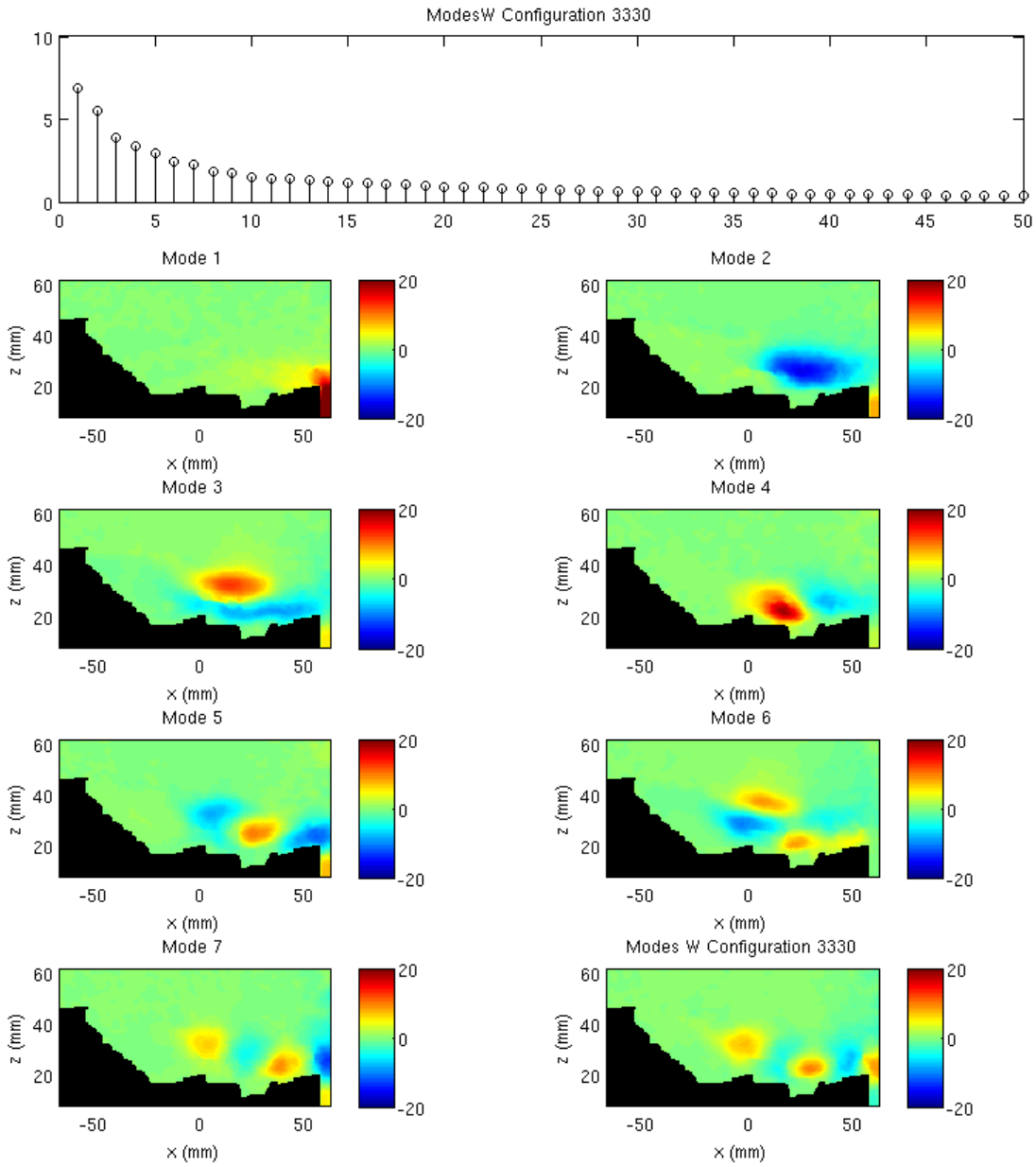

Figure 18: *Contribution (in %) of each λ_n to the total energy and W velocity POD modes for the CLEAN Configuration.*

Annexe 3: Correllations

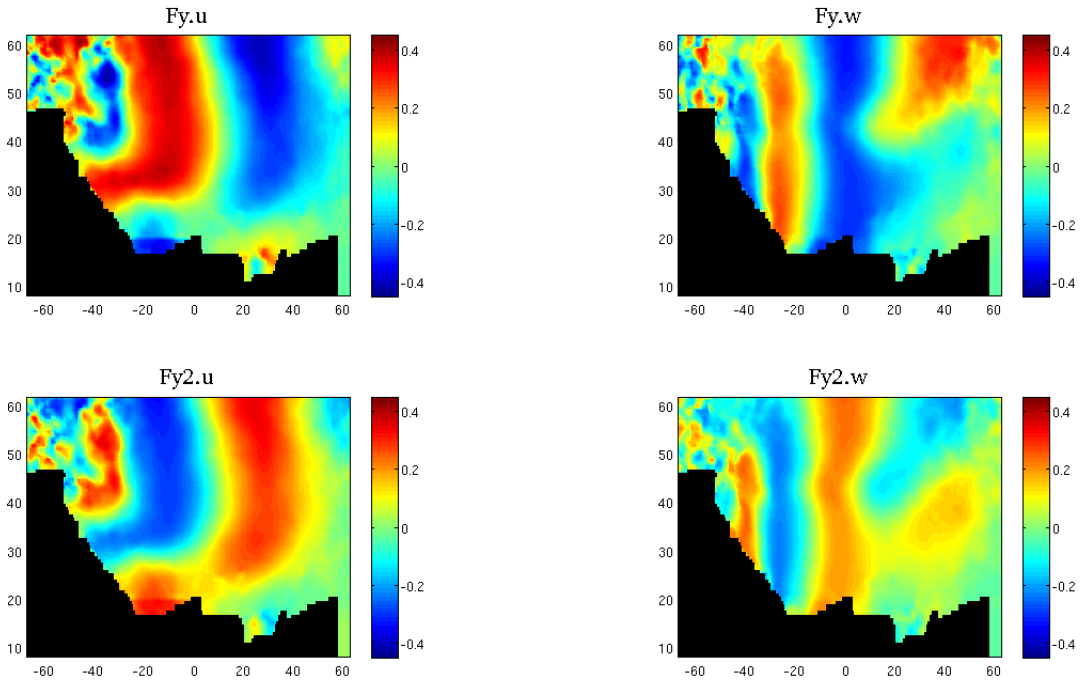

Figure 19: *Correllation coefficient* $[\widehat{C_{Fy}}]_2^5(\boldsymbol{X})$ *for the SMOOTH Configuration.*

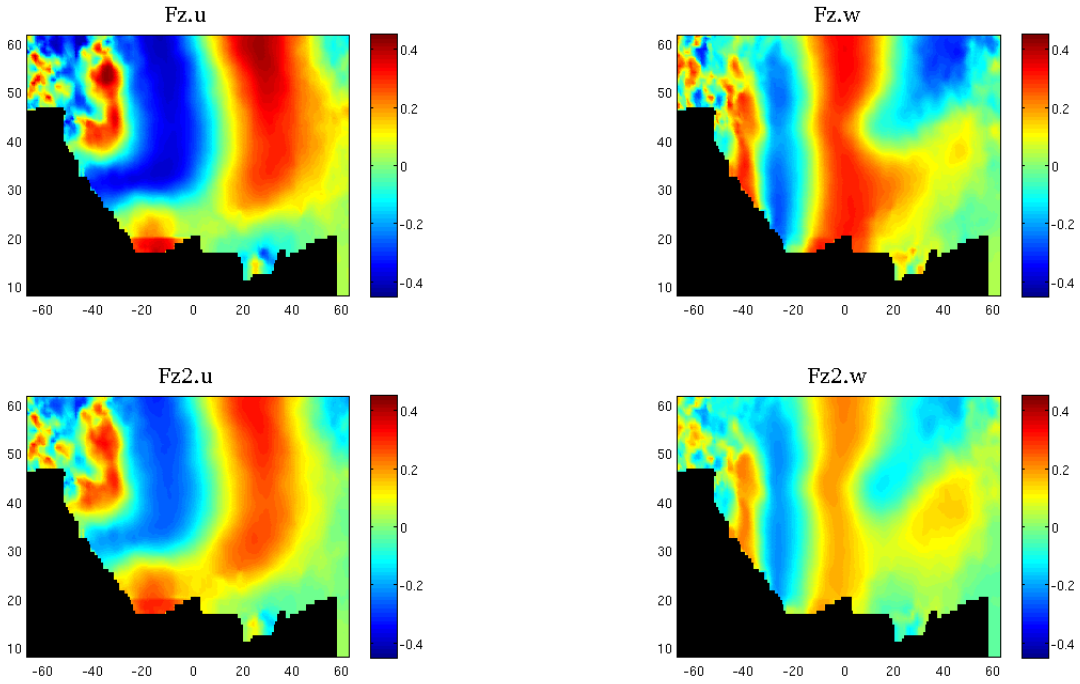

Figure 20: *Correllation coefficient* $[\widehat{C_{Fz}}]_2^5(\boldsymbol{X})$ *for the SMOOTH Configuration.*

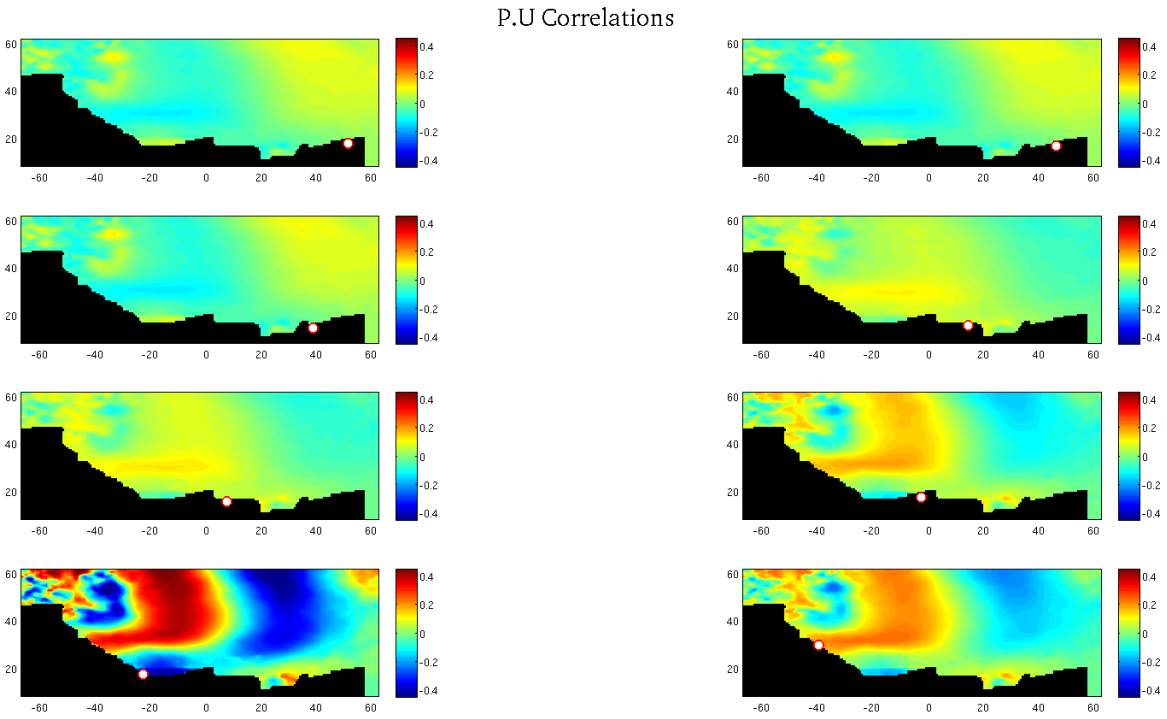

Figure 21: *Correllation coefficient* $[\widehat{C_u^u}]_2^5(\boldsymbol{X})$ *for the SMOOTH Configuration.*

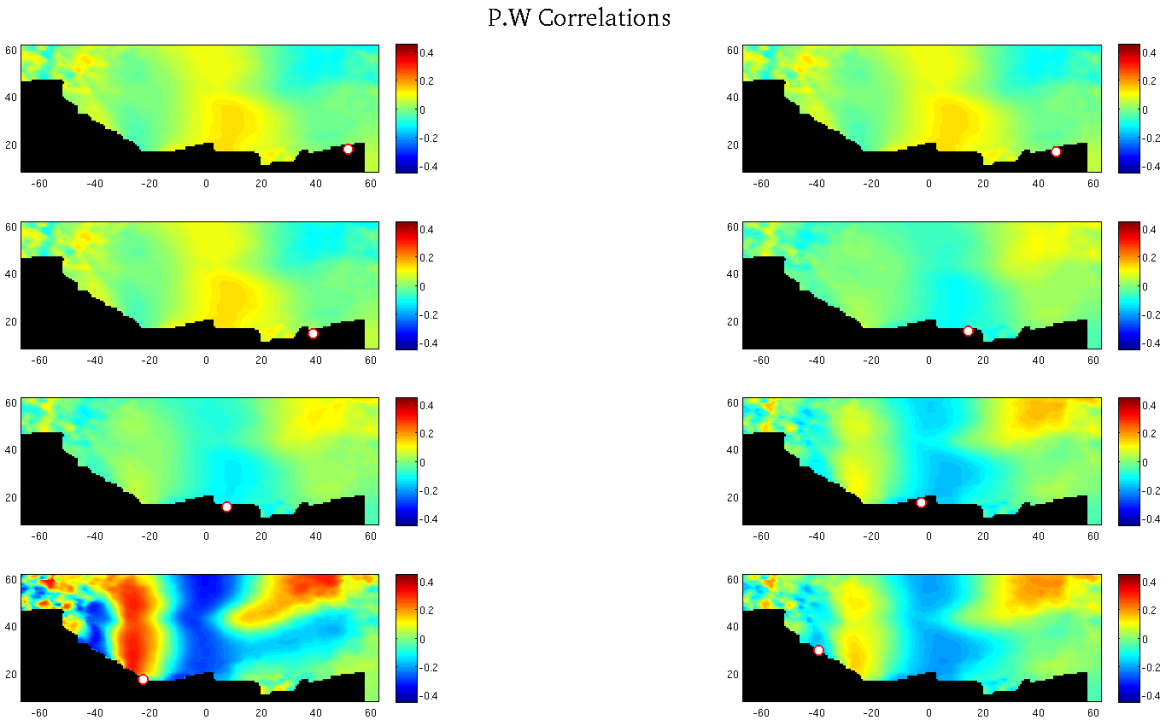

Figure 22: *Correllation coefficient* $[\widehat{C_p^w}]_2^5(\boldsymbol{X})$ *for the SMOOTH Configuration.*

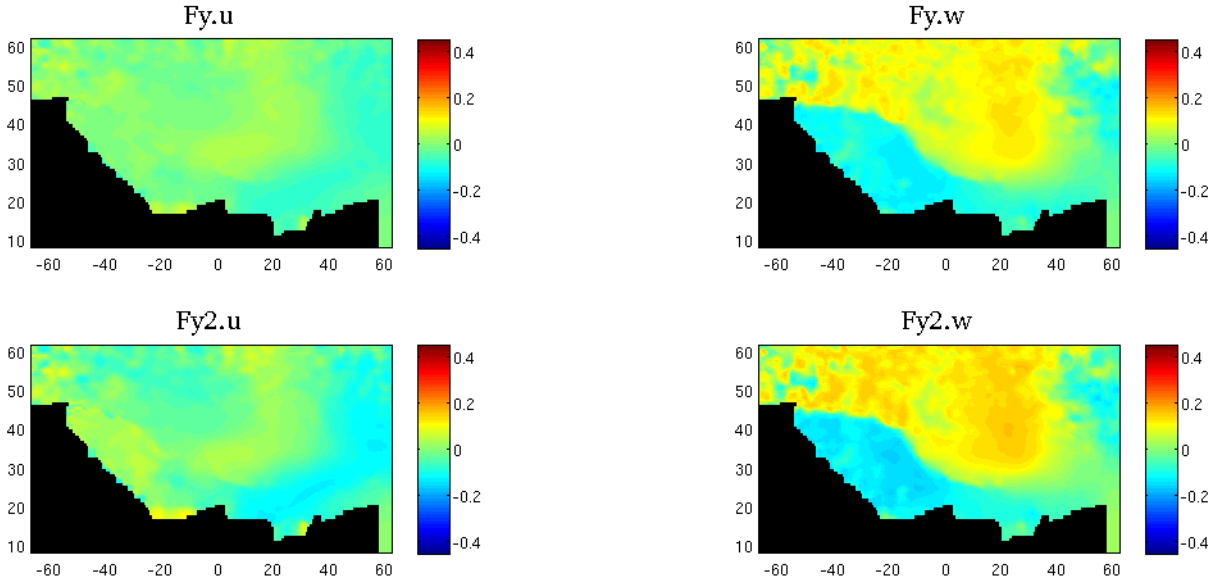

Figure 23: *Correllation coefficient* $[\widehat{C_{Fy}}]_2^5(\boldsymbol{X})$ *for the CLEAN Configuration.*

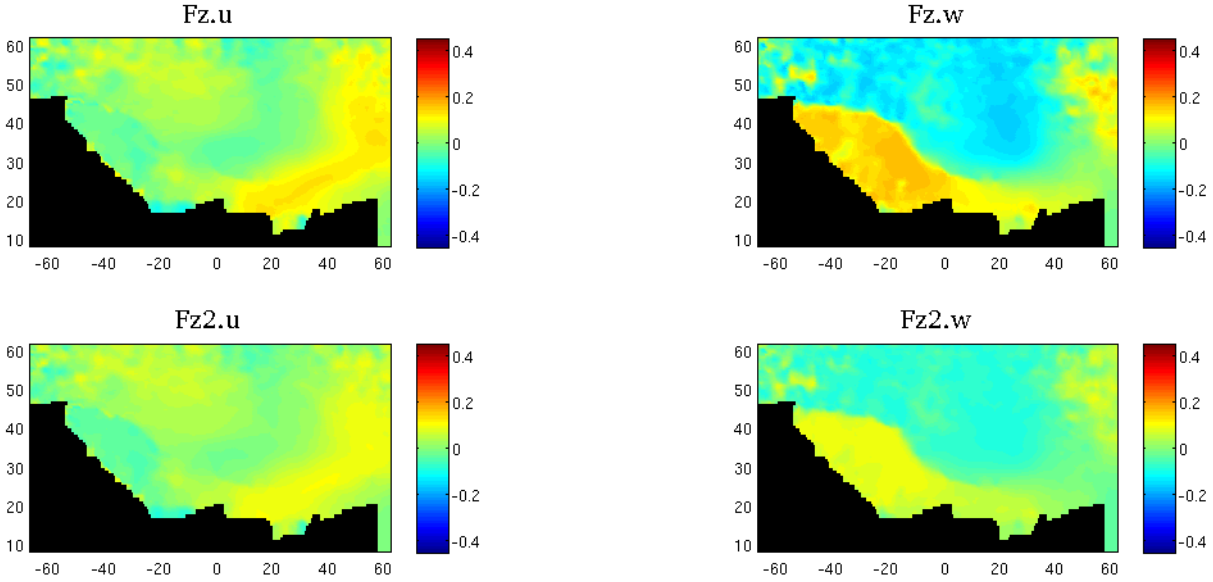

Figure 24: *Correllation coefficient* $[\widehat{C_{Fz}}]_2^5(\boldsymbol{X})$ *for the CLEAN Configuration.*

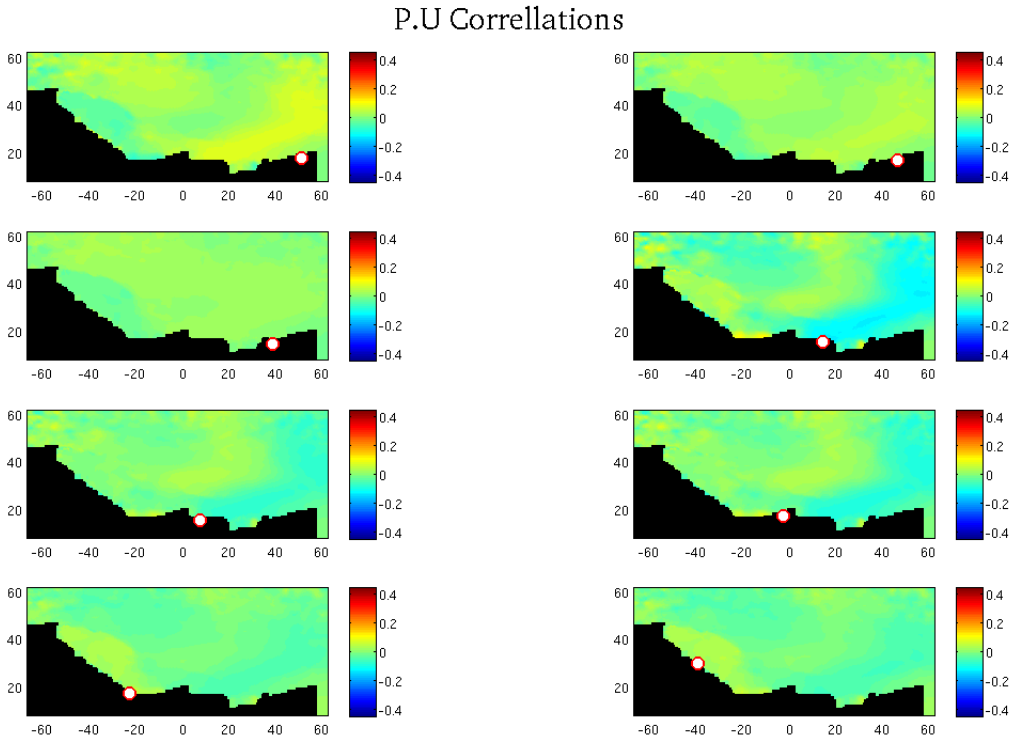

Figure 25: *Correllation coefficient* $[\widehat{C_p^u}]_2^5(\boldsymbol{X})$ *for the CLEAN Configuration.*

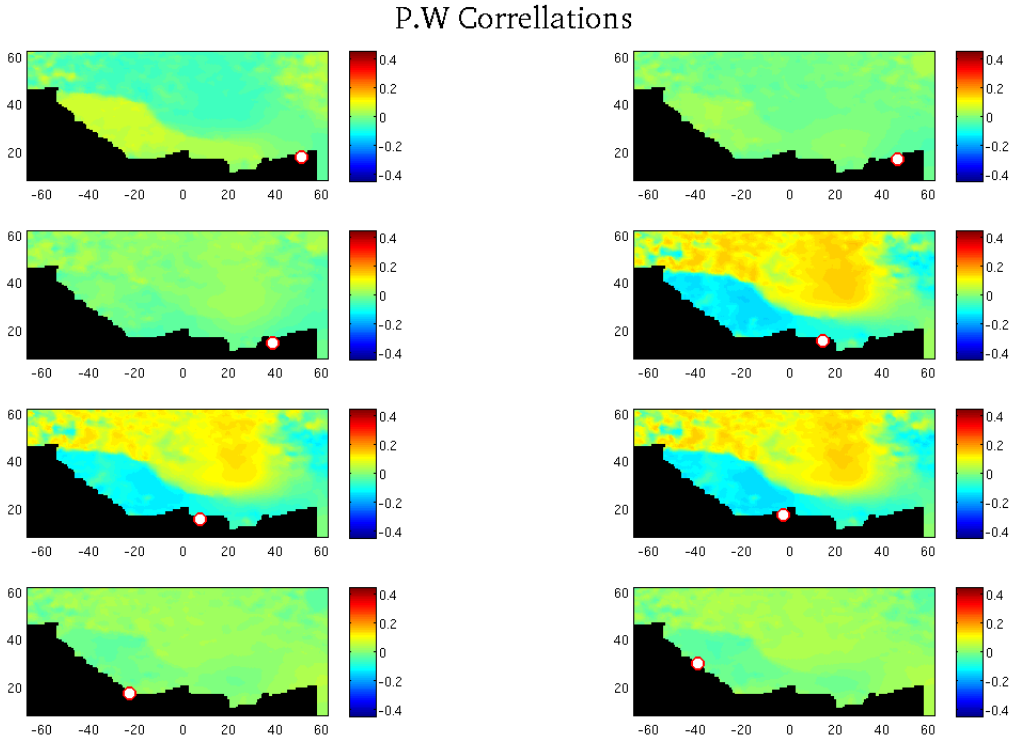

Figure 26: *Correllation coefficient* $[\widehat{C_p^w}]_2^5(\boldsymbol{X})$ *for the CLEAN Configuration.*